

# Glucose Sensing Using Surface-Enhanced Raman-Mode Constraining

Daejong Yang,<sup>†,‡,§</sup> Sajjad Afroosheh,<sup>§</sup> Jeong Oen Lee,<sup>¶</sup> Hyunjun Cho,<sup>¶</sup> Shailabh Kumar,<sup>†</sup> Radwanul H. Siddique,<sup>†</sup> Vinayak Narasimhan,<sup>†</sup> Young-Zoon Yoon,<sup>⊥</sup> Alexey T. Zayak,<sup>\*,§,¶</sup> and Hyuck Choo<sup>\*,†,¶,⊥</sup>

<sup>†</sup>Department of Medical Engineering, California Institute of Technology, Pasadena, California 91125, United States

<sup>‡</sup>Department of Mechanical & Automotive Engineering, Kongju National University, Cheonan 31080, Republic of Korea

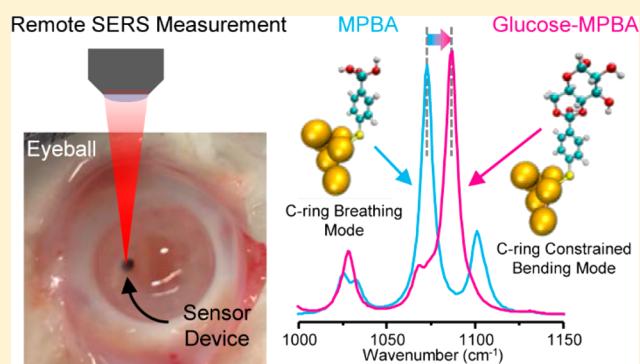
<sup>§</sup>Department of Physics & Astronomy, Center for Photochemical Sciences, Bowling Green State University, Bowling Green, Ohio 43403, United States

<sup>¶</sup>Department of Electrical Engineering, California Institute of Technology, Pasadena, California 91125, United States

<sup>⊥</sup>Device Lab, Device & System Research Center, Samsung Advanced Institute of Technology (SAIT), Suwon 16678, Republic of Korea

## Supporting Information

**ABSTRACT:** Diabetes mellitus is a chronic disease, and its management focuses on monitoring and lowering a patient's glucose level to prevent further complications. By tracking the glucose-induced shift in the surface-enhanced Raman-scattering (SERS) emission of mercaptophenylboronic acid (MPBA), we have demonstrated fast and continuous glucose sensing in the physiologically relevant range from 0.1 to 30 mM and verified the underlying mechanism using numerical simulations. Bonding of glucose to MPBA suppresses the “breathing” mode of MPBA at 1071 cm<sup>−1</sup> and energizes the constrained-bending mode at 1084 cm<sup>−1</sup>, causing the dominant peak to shift from 1071 to 1084 cm<sup>−1</sup>. MPBA–glucose bonding is also reversible, allowing continuous tracking of ambient glucose concentrations, and the MPBA-coated substrates showed very stable performance over a 30 day period, making the approach promising for long-term continuous glucose monitoring. Using Raman-mode-constrained, miniaturized SERS implants, we also successfully demonstrated intraocular glucose measurements in six ex vivo rabbit eyes within ±0.5 mM of readings obtained using a commercial glucose sensor.



Diabetes is a global chronic disease with no cure,<sup>1</sup> requiring frequent monitoring and active management of glucose levels to prevent complications and improve patient outcomes.<sup>2,3</sup> Presently, the glucose level in a body is commonly measured using disposable enzymatic sensors that measure changes in current generated by glucose oxidation in a small sample of blood.<sup>4,5</sup> However, in addition to short shelf-lives because of the intrinsic instability of enzymes and dependence on environmental conditions, the major drawback of these sensors is the painful and inconvenient extraction of blood required for testing.<sup>6–9</sup> Less painful approaches using microneedles for blood extraction or measuring glucose in sweat or the interstitial fluid of skin provide less accurate measurements because of the small sample size or the significantly lower glucose levels in interstitial fluid and sweat compared with in blood.<sup>10–15</sup> Nonenzymatic electrochemical approaches have also been explored to overcome the instability of enzymes; however, these approaches lack specificity for

glucose,<sup>16</sup> and the sensing electrodes develop surface fouling caused by glucose oxidation.<sup>16–18</sup>

Alternatively, optical approaches have been investigated for implementing minimally invasive or noninvasive intensity-based glucose sensing,<sup>19–26</sup> but their use in practical applications has been severely limited by their insufficient sensitivity and low repeatability<sup>19,20</sup> (see the [Supporting Information](#)). Raman spectroscopy is no exception because glucose naturally exhibits weak Raman signals as a result of its small Raman scattering cross-section, measuring only  $5.6 \times 10^{-30}$  cm<sup>2</sup> per molecule per steradian, which is about 14 orders of magnitude smaller than its fluorescence, and glucose's Raman emission is easily overshadowed by strong background noises from the surrounding environment.<sup>25–27</sup> To increase the Raman emission, researchers have employed nanostruc-

Received: July 31, 2018

Accepted: October 28, 2018

Published: October 29, 2018



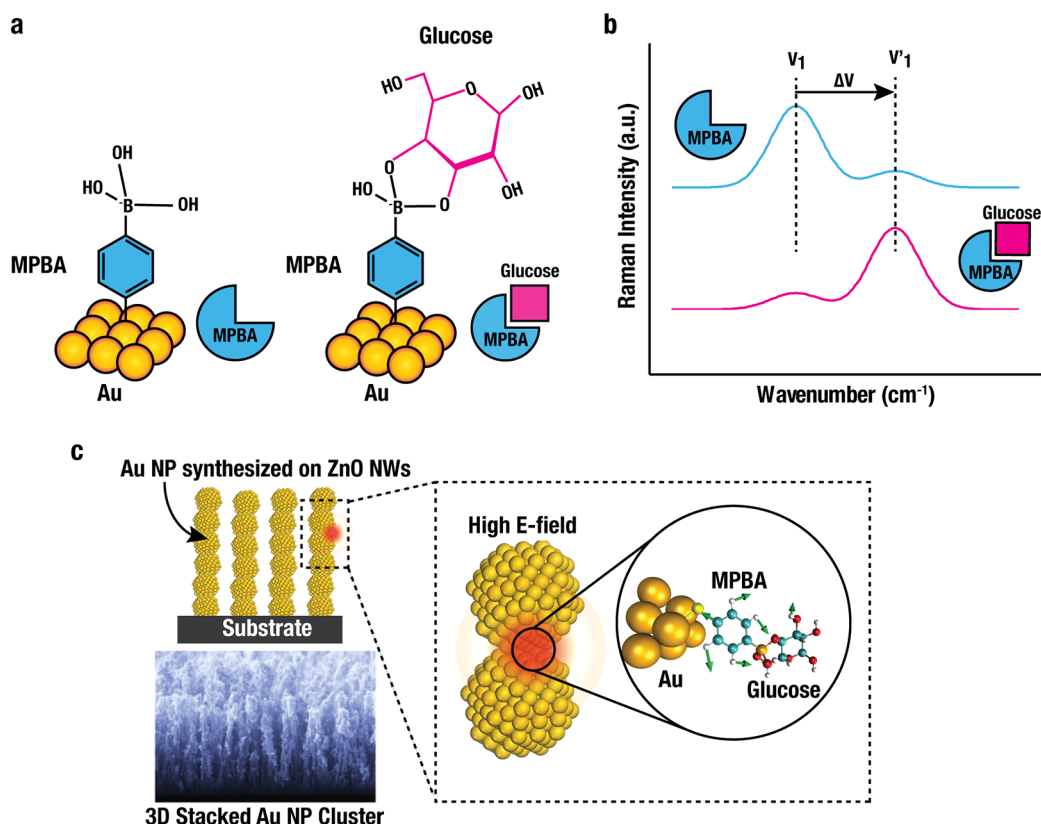


**Figure 1.** Glucose-detection mechanism based on SERS-peak shifting. (a) Schematic illustrations of MPBA (left) and glucose-bound MPBA (right). (b) Shift in the dominant Raman peak of MPBA from  $\nu_1$  to  $\nu_1'$  resulting from glucose binding to MPBA. (c) Schematic illustration and SEM of highly uniform surface-enhanced Raman scattering using 3D Au-NP clusters stacked in a vertical-pillar arrangement.

ture-based surface-enhanced Raman scattering (SERS), which amplifies weak Raman signals by a factor of  $10^6$  to  $10^8$ .<sup>28–32</sup> Because glucose molecules do not possess chemical affinity for SERS-substrate materials such as gold or silver, researchers used decanethiol (DT), mercaptohexanol (MH), and bisboronic acid as SERS-linker molecules and reported glucose detection down to 1 mM.<sup>33–37</sup> However, large linker molecules keep the glucose molecules away from the nearfield enhancement of the substrate surface and make it difficult to achieve more sensitive and consistent measurements.<sup>38–40</sup> Glucose concentrations have also been estimated by detecting increases in the Raman emission of the linker molecule mercaptophenylboronic acid (MPBA) or by comparing relative intensity changes between two adjacent peaks of MPBA when glucose molecules are attached to MPBA.<sup>40,41</sup> The former approach showed little increase in Raman emission, whereas the latter approach was valid only in a highly acidic environment with a pH level close to 1.<sup>40,41</sup>

Here, we demonstrate quantitative, continuous, and rapid sensing of glucose at physiologically observed levels by tracking the shifts in MPBA surface-enhanced Raman-emission peaks. The peak shifts directly result from the bonding of glucose molecules onto the hydroxyl group of MPBA (Figure 1a,b), and we designed the SERS substrates to provide a broad enhancement over the wavelength range of interest (Figure 2).<sup>40</sup> We also identified the underlying mechanism of the Raman-peak shift caused by glucose bonding onto MPBA using numerical simulations (Figure 3) and experimental measurements. Bonding of glucose significantly influences the elasticity of an MPBA molecule, which changes the molecular

geometries and Raman-scattering cross-sections of two C-ring vibrational modes (Figure 3). When a glucose molecule binds, the MPBA-C-ring mode at  $1071\text{ cm}^{-1}$  (Figure 3e) becomes suppressed, while the weakly active C-ring mode at  $1098\text{ cm}^{-1}$  (Figure 3f) changes its vibrational geometry to highly active constrained bending, and shifts its peak location to  $1084\text{ cm}^{-1}$  (Figure 1b). As a result, the position of the hybridized peak between  $1071$  and  $1084\text{ cm}^{-1}$  shifts as a function of the glucose concentration, and using this approach, we measured glucose from 0.1 to 30 mM and, in ex vivo rabbit-eye measurements, demonstrated an accuracy within  $\pm 0.5$  mM of readings obtained using a commercial glucose sensor.

To our knowledge, Raman-peak shifting has previously been utilized for several sensing applications,<sup>42–46</sup> yet tracking a Raman-peak shift that results from Raman-mode constraining has not been used for glucose sensing. Furthermore, tracking the SERS-peak shift proves to be a more reliable and consistent method to measure glucose concentrations than intensity-based SERS-sensing approaches.<sup>44</sup> SERS-emission intensity is directly influenced by the enhancement factors of the SERS substrates, which typically show large spatial and chip-to-chip fluctuations, whereas the positions of the Raman-emission peaks are determined by the vibrational states of the molecules and are highly independent of the enhancing performance of individual substrates.<sup>46</sup> Moreover, boronic acid is a biocompatible molecule,<sup>47–49</sup> and its covalent bonding with glucose is rapid and also reversible,<sup>50,51</sup> making our approach potentially promising for an in vivo continuous sensing applications.

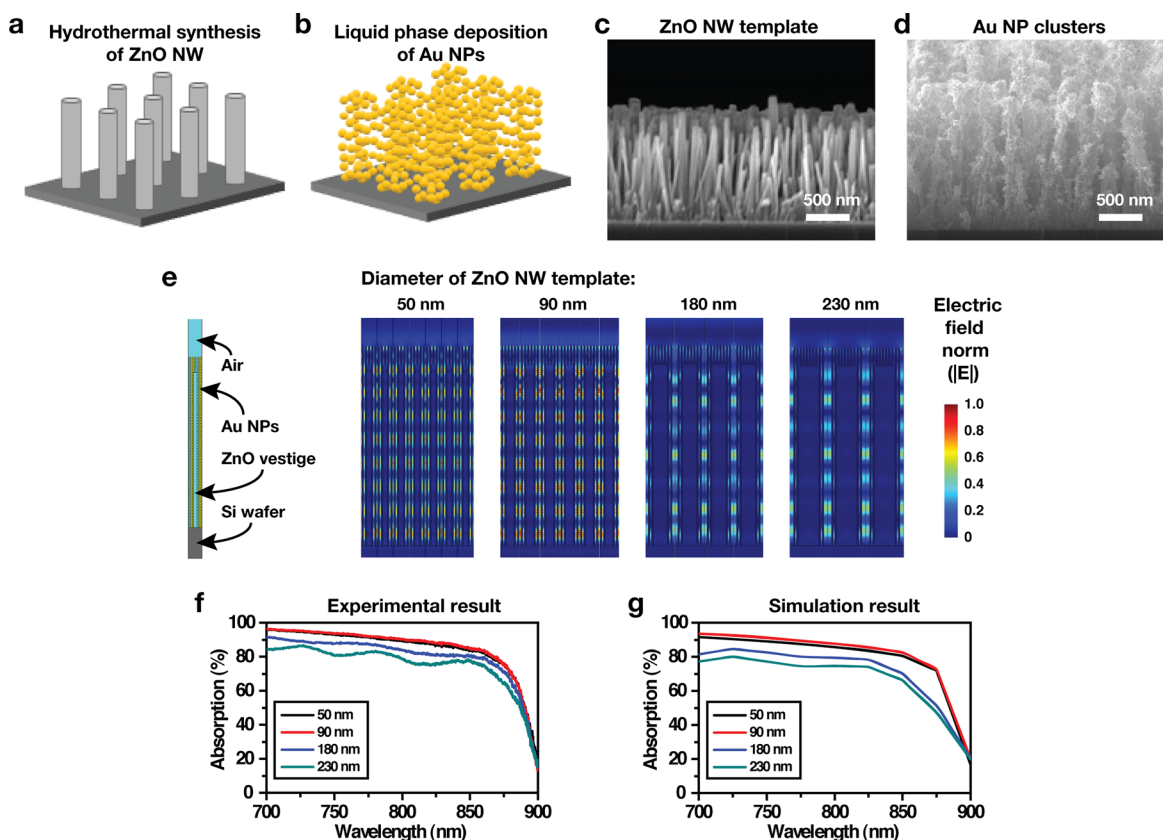


**Figure 2.** Fabrication and properties of the SERS substrate. (a) ZnO NWs fabricated on a Si substrate using hydrothermal synthesis. (b) 3D Au NPs deposited in a pillar-array format using liquid-phase deposition. (c,d) SEM images of (c) ZnO-NW template and (d) 3D Au-NP clusters. (e) Electric-field norm ( $|E|$ ) of the 3D-stacked-Au-NP-cluster SERS substrate with various diameters of ZnO-NW templates. (f) Experimental and (g) simulation results of the absorption of the SERS substrates made with ZnO NWs of four different diameters.

## RESULTS AND DISCUSSION

For SERS-substrate fabrication, we selected a fabrication process previously developed for strong Raman enhancement and excellent spatial uniformity<sup>52,53</sup> and further engineered the process to produce substrates optimized for this glucose-sensing application, providing excellent broadband SERS response over the relevant spectral range from 785 nm (the excitation-laser wavelength) to 858 nm (or  $1084\text{ cm}^{-1}$ , the target glucose Raman emission).<sup>28</sup> The fabrication was performed in a two-step process: (1) hydrothermal synthesis of ZnO nanowires (NWs, Figure 2a) and (2) liquid-phase deposition of Au nanoparticles (NPs) on the ZnO NWs (Figure 2b).<sup>52</sup> The ZnO NWs produced in the first step serve as skeletal frames for Au-NP deposition, determining the periodicity, width, and height of the final Au-NP pillars and gradually dissolving away during the second processing step, leaving hollow, vertical perforations that serve as light passages (Figures 2c,d and S1c). To find the optimal geometry for the SERS substrates, we varied the concentration of zinc nitrate hexahydrate in the presence of the nanowire-growth-limiting hexamethylenetetramine (HMTA) in the precursor solution during the first processing step; synthesized ZnO nanowires of four different diameters, 50, 90, 180, and 230 nm (Figure S1a); and performed the near-infrared-absorption spectroscopy and finite-element simulations (Figure 2e–g). The results show that the substrates with 50 nm ZnO NWs provide almost constant broad absorption (>85%) over the relevant spectral range between 785 and 858 nm, which can also be confirmed by the pitch-black appearance of the processed wafer (Figure

S1d).<sup>28,52</sup> The fabricated substrate also exhibited a high Raman-enhancement factor of around  $9.31 \times 10^9$  and excellent uniformity, indicated by the low relative standard deviation (RSD) below 4% over a  $1 \times 1\text{ mm}$  area (see the Supporting Information and Figure S1e,f).<sup>52</sup>

Using the fabricated substrates, we measured SERS spectra of 1 mM MPBA in pure phosphate-buffered-saline (PBS) solution and PBS containing 10 mM glucose (Figure S2a). In both cases, two major peaks were observed between 1070 and  $1075\text{ cm}^{-1}$  and between  $1570\text{--}1580\text{ cm}^{-1}$ . The former is the “breathing” mode assigned to C–S stretching coupled with C–ring expansion, and the latter is a mode assigned to B–C stretching coupled with C–C in-ring stretching.<sup>41,54</sup> For the double-peak structure between  $1570\text{ and }1580\text{ cm}^{-1}$ , the low- and high-frequency peaks correspond to MPBA with three and two hydroxyl groups, respectively (Figure S2b,c). MPBA naturally has two hydroxyl groups. When MPBA is exposed to mildly basic (alkaline) conditions (e.g., pH 7.4 PBS solution), the molecule acquires an additional hydroxyl group to form a ( $\text{OH}^-$ )-MPBA ion, which has been reported to have a higher affinity for bonding with glucose.<sup>41,55</sup> Our numerical simulations showed that the two forms of MPBA behave similarly with regard to the glucose-detection mechanism reported in this work, and we consider the three-hydroxyl-group structure for the following discussions. When the MPBA-assembled substrate was immersed in the 10 mM glucose solution, the measured peak at  $1071.5\text{ cm}^{-1}$  shifted to  $1072\text{ cm}^{-1}$  (Figure S2d) because of changes in the dominant-peak intensities.



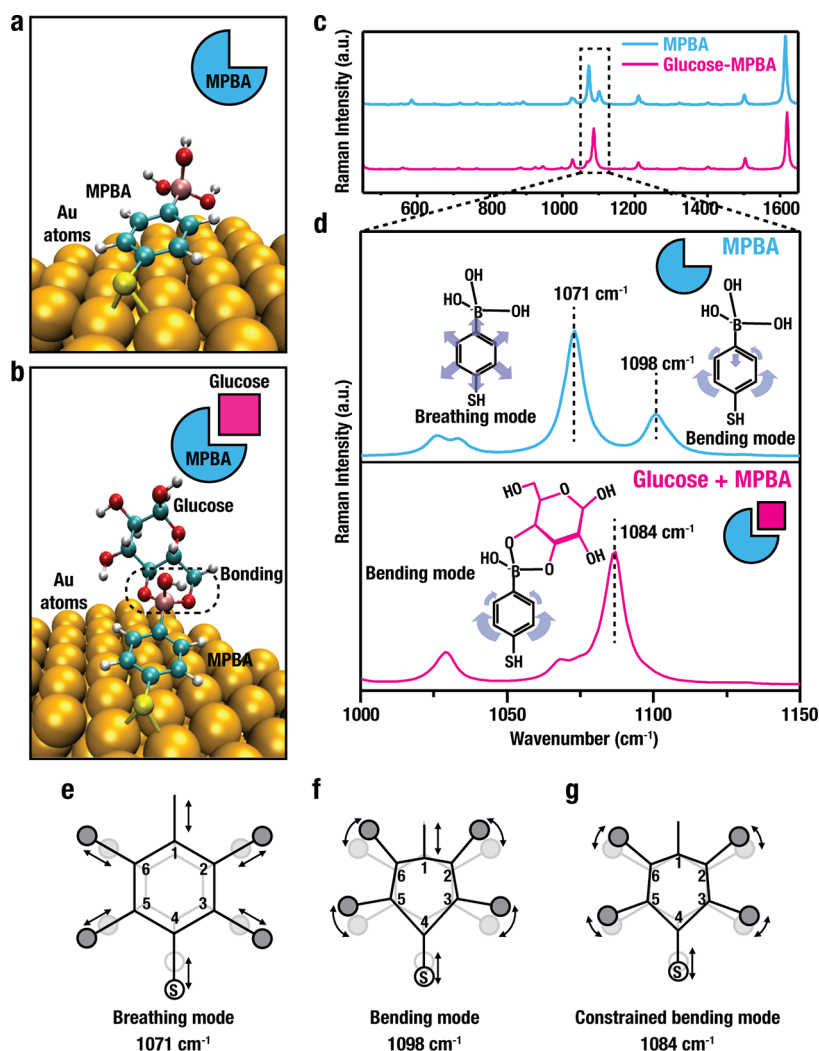


**Figure 3.** Analysis of SERS-peak shifts using numerical simulations based on density functional theory (DFT). (a,b) DFT-simulation geometries used for studying  $(\text{OH}^-)$ -MPBA's Raman-peak-shifting mechanism (a) before glucose binding and (b) after glucose binding. (c) DFT-simulation of  $(\text{OH}^-)$ -MPBA and  $(\text{OH}^-)$ -MPBA-glucose SERS spectra in mildly basic (pH 7.4) PBS. (d) SERS spectra of MPBA showing the C–S-stretching-coupled C-ring-breathing mode at  $1071\text{ cm}^{-1}$ , the C–S-stretching-coupled C-ring-bending mode at  $1098\text{ cm}^{-1}$ , and the glucose-bound C–S-stretching-coupled C-ring-constrained-bending mode at  $1084\text{ cm}^{-1}$  along with molecular structures indicating the vibrational motions. (e–g) Schematic diagrams showing the in-plane C-ring vibrational modes of  $(\text{OH}^-)$ -MPBA: (e) breathing mode at  $1071\text{ cm}^{-1}$ , (f) bending mode at  $1098\text{ cm}^{-1}$ , and (g) constrained-bending mode of glucose-bound  $(\text{OH}^-)$ -MPBA at  $1084\text{ cm}^{-1}$ .

The peak-shifting mechanism can be explained by performing a series of numerical simulations of the SERS spectra of MPBA with and without bonding glucose (Figure 3). MPBA or  $(\text{OH}^-)$ -MPBA attaches to the Au substrate using a thiol group (Figure 3a), and glucose bonds to the hydroxyl group of MPBA through a dehydration reaction (Figure 3b). Two of the three hydroxyl groups of  $(\text{OH}^-)$ -MPBA bond with glucose, and the third is left unoccupied. Figure 3c,d shows SERS spectra of  $(\text{OH}^-)$ -MPBA and glucose-bound  $(\text{OH}^-)$ -MPBA obtained using density-functional-theory (DFT) simulations. For both MPBA and  $(\text{OH}^-)$ -MPBA without glucose, two large peaks were observed at  $1071$  and  $1098\text{ cm}^{-1}$ . The peak at  $1071\text{ cm}^{-1}$  is dominant in this scenario and originates from the coupled C–S-stretching and the C-ring-breathing motions shown in Figure 3e. The peak at  $1098\text{ cm}^{-1}$  is assigned to the C–S stretching coupled with the C-ring-bending motion (shown schematically in Figure 3f). In the case of glucose-bonded  $(\text{OH}^-)$ -MPBA, the peak assigned to the C-ring-breathing mode becomes negligible, while the C-ring-bending-

mode peak becomes dominant and redshifts to  $1084\text{ cm}^{-1}$ , because of the constraint imposed by glucose (Figure 3g). Overall, the bonding of glucose shifts the dominant Raman peak from  $1071$  toward  $1084\text{ cm}^{-1}$ . The molecular structures in Figure 3e–g and the Supplementary Video show the three motions discussed: (1) C–S-stretching-coupled C-ring-breathing mode of  $(\text{OH}^-)$ -MPBA, (2) C–S-stretching-coupled C-ring-bending mode of  $(\text{OH}^-)$ -MPBA, and (3) C–S-stretching-coupled C-ring-constrained-bending mode of  $(\text{OH}^-)$ -MPBA bound with glucose.

The theoretical results matched the experimental results; however, the magnitudes of the peak shift in the simulations were larger than in the experimental data because of the inherent approximations of the DFT method. In the experimental-measurement environment, unoccupied MPBA molecules are expected to coexist with glucose-bound  $(\text{OH}^-)$ -MPBA molecules in the laser-probing spot, and the location of the peak will be an average of the unoccupied-MPBA-molecule and glucose-bound- $(\text{OH}^-)$ -MPBA-molecule peaks. If the ratio

of glucose-bound ( $\text{OH}^-$ )-MPBA to unoccupied MPBA increases, the peak will shift closer to the theoretical value of  $1084\text{ cm}^{-1}$ .

Glucose bonding can also affect the B–C-stretching-coupled C–C-stretching mode of MPBA near  $1580\text{ cm}^{-1}$  in a highly acidic environment with a pH close to 1.<sup>40</sup> We have verified, however, that this change does not occur in our mildly basic environment using pH 7.4 PBS solution (Figure S2e). In addition, we also verified that it is difficult to directly observe the SERS peaks of glucose molecules. As shown in Figure S2fg, no peaks were observed at the expected locations indicated by the blue arrows up to 10 mM glucose.<sup>35</sup> Collectively, these results supported tracking the  $1071\text{ cm}^{-1}$  MPBA SERS peak to provide a more accurate and reliable method to detect glucose concentrations.

In order to experimentally correlate peak-shift behavior to glucose concentration, SERS spectra of MPBA were measured in the presence of 0.1–30 mM glucose in PBS. This measurement range covers low glucose concentrations found in the aqueous humor of healthy adults as well as high concentrations observed in diabetic blood samples.<sup>56–58</sup> The measurements were performed inside the polydimethylsiloxane (PDMS) chamber as shown in Figure S3. The plots in Figure 4a,b show the positions of the hybridized SERS peak as a function of glucose concentration varying from 0.1 to 30 mM in PBS. As discussed earlier, this hybridized peak results from MPBA's C–S-stretching-coupled C-ring-breathing and -bending modes that are significantly influenced by glucose bonding and are easily observed because of their large combined emission intensity. Figure 4a shows SERS spectra of MPBA in the presence of glucose concentrations ranging from 0 to 30 mM. The spectra were normalized with respect to the highest peak around  $1071.5\text{ cm}^{-1}$ . The initial peak position of MPBA in PBS was  $1071.5\text{ cm}^{-1}$ , and it shifted toward larger wave numbers as the glucose concentration was increased (Figure 4b). Figure 4c shows the peak position of MPBA logarithmically increasing with increasing glucose concentrations.

Figure 4d shows the initial dynamic response of our peak-shifting approach when measured in PBS with 0.1, 1, and 10 mM glucose. We applied an additional Savitzky–Golay filter in the time domain (see the Materials and Methods section and Figure S5). Upon injecting the glucose solution into the measurement chamber, the hybridized peak began to shift to the right, and its position approached the saturation point over a period. For higher glucose concentrations, the peak shifting and saturation occurred more rapidly when the concentration reached 10 mM.

The reaction between MPBA and glucose and the relationship between the peak wavenumbers follow the first-order reaction-rate equation:<sup>49</sup>

$$W_n = W_0 + A(\exp(-t/\tau) - 1) \quad (1)$$

where  $W_n$ ,  $W_0$ ,  $A$ ,  $t$ , and  $\tau$  represent the peak wavenumber in glucose solution, the peak wavenumber in PBS solution, the real constant, time, and the time constant, respectively. As the glucose concentration increases, the rate of peak shift increases. We formulated an analytical glucose-sensing model to predict the device response at various concentrations ranging from 0–30 mM (see the Supporting Information and Figure S5 for more details).

The standard way to estimate the glucose concentration using Raman-mode constraining is to measure the peak shift directly after the reaction has reached an equilibrium and the

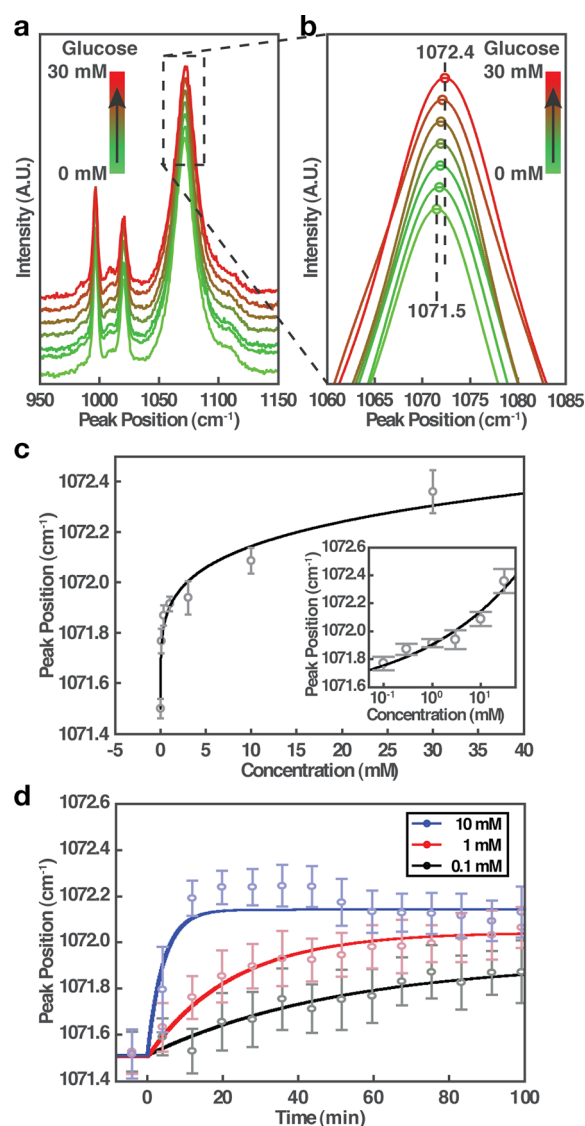


**Figure 4.** Measuring glucose concentrations by tracking Raman-peak positions. (a) Normalized SERS spectra of MPBA in the presence of glucose concentrations ranging from 0 to 30 mM. (b) Magnified view of SERS peaks near  $1071\text{ cm}^{-1}$  for glucose concentrations from 0 to 30 mM. (c) SERS-peak position vs glucose concentration for glucose concentrations between 0 and 30 mM. (d) Initial dynamic shifting of SERS-peak positions vs time when 0.1, 1, and 10 mM glucose solutions are applied at  $t = 0$ . Initial slopes are a function of glucose concentration and are distinct at each concentration.

peak position has almost been finalized. The measurement speed of this method requires approximately 10 to 30 min depending on the glucose concentration (Figure S5a–c). Predicting the concentration from the initial slope of the peak shifting is accurate and fast, which can be completed within 1 min. For systems that start from a standard baseline or where the initial glucose concentration ( $C_{\text{initial}}$ ) is known, the slope method can be as accurate as the peak-position shift, as shown in Figure S5. A stand-alone-slope method has not been tested for dynamically changing environments because it requires prior knowledge of  $C_{\text{initial}}$  to improve the estimation of  $C_{\text{final}}$ . Extensive comparisons between the final-peak-shift and initial-slope methods as well as a combination of these two methods in dynamically changing environments will be pursued in the future, building upon the work presented in this manuscript.

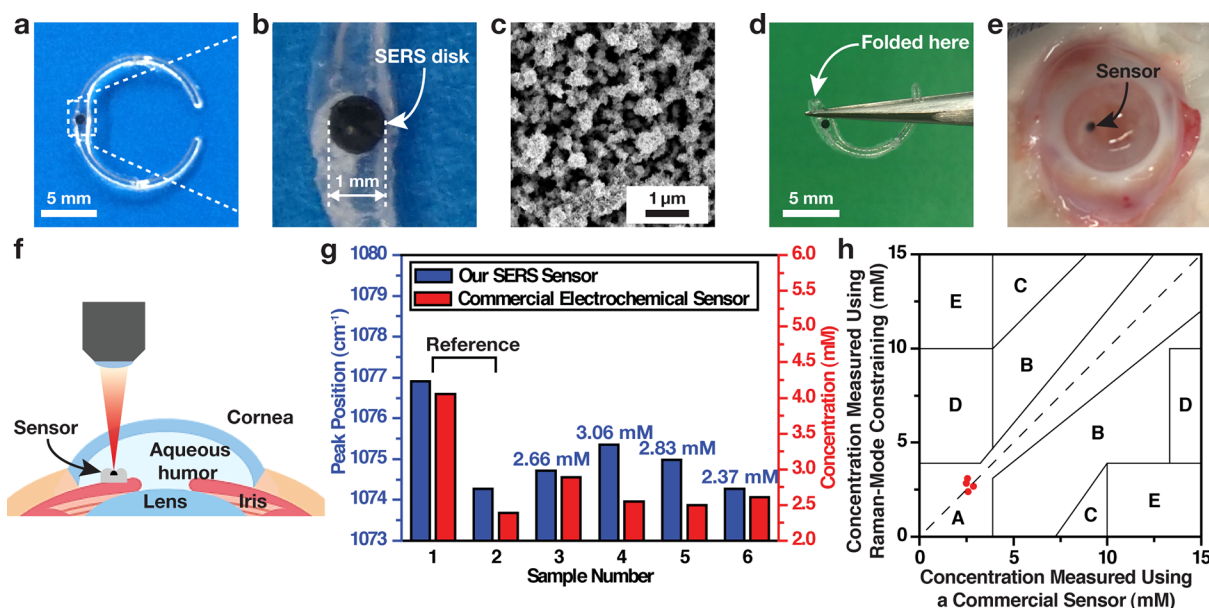


**Figure 5.** Measuring glucose concentrations in the aqueous humor of ex vivo rabbit eyes. (a) Photo of the SERS-disk-mounted C-shaped implant made of PDMS. The loop diameter is 10 mm, the circular-shaped beam is 1 mm wide, and the mounting region is 1.5 mm wide. (b) Photographic image of a SERS disk. (c) SEM image of 3D-stacked Au-NP clusters fabricated on the SERS disk. (d) Photo of the folded SERS-disk-mounted implant. (e) Photo of the implant inserted inside the anterior chamber of an ex vivo rabbit eye. (f) Schematic illustration of the glucose measurement made using the SERS implant inside the anterior chamber of an ex vivo rabbit eye. (g) Glucose-concentration measurements made using our Raman-mode-constraining approach (blue) in comparison with readouts concurrently obtained using a commercial electrochemical glucose sensor (red). The first two measurements (1 and 2, blue) made using Raman-mode constraining served as references to calculate the other four measurements (3–6), and the corresponding glucose concentrations are displayed in blue over the bars in the histogram. (h) Clarke-error-grid analysis of the glucose measurements using our Raman-mode-constraining approach in ex vivo rabbit eyes.

Next, we tested our approach for its reversibility and ability to track ambient glucose concentrations, important factors for continuous monitoring. The weak association constant of phenylboronic acid with glucose ( $4.6 \text{ M}^{-1}$  at pH 7.4)<sup>59</sup> is advantageous for real-time continuous sensing of concentrations of glucose. Glucose molecules maintain a dynamic equilibrium between association and disassociation with MPBA, allowing continuously changing glucose concentrations in solution to be monitored. We performed dynamic-response testing by placing an MPBA-coated chip in the PDMS test chamber and alternating the ambient solution between PBS and 10 mM glucose PBS solutions. When the glucose solution was injected into the chamber, the peak shifted to a larger wavenumber, and when the glucose line was turned off and the PBS solution line was turned on, the peak returned to the initial location. Because of the relatively weak bonding force between MPBA and glucose, our approach showed reversible peak shifting and continuous monitoring of the glucose concentration, as shown in Figure S5g.<sup>49–51,59</sup>

Achieving reliable and stable measurements over an extended period is an important criterion for the practical application of sensors, especially implantable devices. Hence, we tested the long-term usability of our approach by measuring the SERS-peak locations in a 10 mM glucose PBS solution for one month. As shown in Figure S6, the device produced a very stable sensing result during the test period. The average daily drift of the peak position over this period was  $-0.0006 \text{ cm}^{-1}$  per day, which is highly encouraging for long-term continuous glucose monitoring.

Fructose, which has five hydroxyl groups, can also bond with MPBA in a similar manner and shift MPBA's Raman peak.<sup>60,61</sup> However, the concentrations of fructose observed in aqueous

humor, urine, and blood are typically  $10^{-3}$  to  $10^{-2}$  times those of glucose,<sup>56,62,63</sup> and thus, its influence on our glucose measurement is considered negligible.

As a feasibility study, we measured glucose concentrations in the aqueous humor of fresh ex vivo rabbit eyes using the Raman-mode-constraining approach. Eyes are light-friendly biological structures suitable for optical sensing. In addition, we used polydimethylsiloxane (PDMS) to fabricate the implant mount for our SERS disks. PDMS is a biocompatible material<sup>64,65</sup> and has been utilized for the fabrication of implantable medical devices as well as ocular implants in the past.<sup>66–68</sup> In the ciliary body, the aqueous humor is produced by diffusion and ultrafiltration of blood plasma through the ciliary body.<sup>69</sup> As a result, the glucose concentration in the aqueous humor follows the blood glucose level more consistently and closely than other bodily fluids such as tears.<sup>56–58,69,70</sup> The glucose range of 0.1–30 mM in the aqueous humor corresponds to 0.1–60 mM in blood, which covers the physiologically relevant glucose levels observed in normal and diabetic conditions.

The anterior chambers of human eyes have emerged as the optimal site for compact, minimally invasive medical implants, providing easy optical accessibility for convenient and remote monitoring of various aspects of human health.<sup>71</sup> For ex vivo measurements, we fabricated C-shaped PDMS implants mounted with SERS disks (see Figure 5a–c and the Materials and Methods section). The C-shaped PDMS, measuring 1 mm in width, is elastic and flexible, it can be folded in half as shown in Figure 5d. This allowed for insertion through a small incision in the cornea, and when released, the folded implant self-restored back to its original C shape and positioned itself inside the anterior chamber as shown in Figure 5e (see the



Materials and Methods section and Figure S7). We performed the ex vivo eye measurements as shown in Figure 5f. The SERS implants were positioned about halfway between the center and the edge of the cornea (Figure 5e), and the optical transmittance of a fresh rabbit cornea is over 90% between 520 and 870 nm.<sup>72</sup> The laser light passes through the cornea and reaches the SERS disk placed off the optical axis of the eye, mainly exposing the cornea to the laser light. Risk of thermally damaging the cornea is minimal because the cornea has high transmittance (over 95% at 785 nm), and the tissues show minimal absorption at 785 nm.<sup>72</sup> We measured the glucose concentrations of the rabbit aqueous humor using the SERS implants, and compared the values with concurrently obtained readouts from a commercially available electrochemical glucose sensor, finding an accuracy of  $\pm 15\%$  in 99% of the measurements for glucose concentrations above 4 mM (Figure 5g). All of the data measured by the implanted sensor were located in region A of the Clarke error grid (Figure 5h). Our SERS sensors produced robust Raman peaks with high intensities and positions that were easily tracked. Our Raman-mode-constraining approach produced measurements that matched the readouts concurrently obtained from the commercial sensor within 0.5 mM. This error range is acceptable for use with diabetic patients,<sup>73</sup> whose glucose concentrations typically vary on the order of 10 mM.

## MATERIALS AND METHODS

**Chemicals.** Chemicals used in this work include zinc acetate dihydrate ( $\text{Zn}(\text{CH}_3\text{COO})_2 \cdot 2\text{H}_2\text{O}$ , Sigma Aldrich,  $\geq 98\%$ ), ethanol ( $\text{CH}_3\text{CH}_2\text{OH}$ , Sigma Aldrich, 200 proof), zinc nitrate hexahydrate ( $\text{Zn}(\text{NO}_3)_2 \cdot 6\text{H}_2\text{O}$ , Sigma Aldrich, 98%), polyethyleneimine (PEI,  $(\text{C}_2\text{H}_5\text{N})_m$ , Sigma Aldrich, average MW  $\sim 800$ ), hexamethylenetetramine (HMTA,  $\text{C}_6\text{H}_{12}\text{N}_4$ , Sigma Aldrich,  $\geq 99\%$ ), sodium tetrachloroaurate(III) dihydrate, ( $\text{NaAuCl}_4 \cdot 2\text{H}_2\text{O}$ , Sigma Aldrich,  $\geq 99\%$ ), sodium citrate dihydrate ( $\text{HOC}(\text{COONa})(\text{CH}_2\text{COONa})_2 \cdot 2\text{H}_2\text{O}$ , Sigma Aldrich,  $\geq 99\%$ ), sodium hydroxide (NaOH, Sigma Aldrich,  $\geq 98\%$ ), 4-mercaptophenylboronic acid (MPBA,  $\text{HSC}_6\text{H}_4\text{B}(\text{OH})_2$ , Sigma Aldrich, 90%), and phosphate-buffered saline (PBS, Sigma Aldrich, pH 7.4).

**Design and Fabrication of Broadly Enhancing 3D-Stacked Au-NP SERS Substrates.** The SERS substrates were fabricated by performing two sequential wet-chemical processes described in detail by Yang et al.<sup>52</sup> A bare silicon (Si) substrate was coated with a ZnO seed, and the seeded substrates were then dipped into the ZnO precursor solutions and heated in a convection oven at  $95^\circ\text{C}$  for 2.5 hours (Figure 2a). The ZnO nanowire substrates were dipped into the Au-NP precursor solution and heated for 1 hour at  $90^\circ\text{C}$  in a convection oven. The Au-NP deposition process was repeated five times to achieve densely formed 3D-stacked Au-NP clusters. During these iterations, the ZnO nanowires initially served as 3D frames for Au-NP deposition and gradually dissolved (Figure 2b, see Section 1 of the Supporting Information).

**Optical Simulations of the SERS Substrates.** Two-dimensional (2D) modeling of the SERS devices (Figure 2e) was performed using the finite-element-method (FEM) software COMSOL Multiphysics. The effective dimeters and periods of the devices were extracted from the scanning-electron-microscopy (SEM) images. The periodic boundary condition and normal incidence for transverse magnetic (TM)

polarization were used (see Section 1 of the Supporting Information).

**Near-Infrared Spectroscopy of the SERS Device.** A customized optical microscope operating in bright-field (BF) mode was used for the absorption measurement of the fabricated samples. A halogen lamp was used as a light source with a  $50\times$  objective, and reflected light ( $R$ , %) was collected in a confocal configuration using a  $1000\ \mu\text{m}$  core optical fiber and analyzed using a mini spectrometer (Maya200 Pro, Ocean Optics). The absorption ( $A$ , %) was calculated from the reflected light ( $100 - R$ ) considering null transmission.

**Density-Functional-Theory (DFT) Simulation for Raman Peak Shift.** Raman calculations were carried out using the Gaussian '09 software package.<sup>74</sup> All calculations were performed using the DFT method with the hybrid B3LYP exchange correlation functional.<sup>75</sup> The 6-311++g(d,p) and Stuttgart–Dresden (SDD) basis sets were used for the molecule–metal systems. The SDD numerical basis was used to treat more accurately the core electrons of gold via the effective core potentials (ECP), which included relativistic effects<sup>76</sup> (see Section 1 of the Supporting Information).

**Assembly of Linker Molecules on the SERS Substrate.** The substrates were incubated in a 1 mM 4-MPBA solution for 5 hours. Then, the substrates were fully rinsed with ethanol and dried using a nitrogen gun.

**Bench-Top Measurement of Glucose Concentration.** The substrates were placed inside a chamber made of polydimethylsiloxane (PDMS, Sylgard 184, Dow Corning), and the chamber (with inner dimensions of 2 mm in height, 2 mm in width, and 8 mm in length) was covered with a fused-silica cover slip (S1-UV, ESCO Products Inc.) that served as a measurement window (Figure S3). Various concentrations of glucose–PBS solutions were delivered by using a syringe-pump system (NE-500, New Era Pump Systems Inc.). SERS signals were measured using a Raman spectrometer (inVia confocal Raman microscope, Renishaw) with a  $5\times$  objective and a 785 nm laser operating at 0.8 mW (see Section 1 of the Supporting Information).

**Raman-System Spectral Resolution and Data Processing.** To improve the spectral accuracy, we employed the well-established data-processing method used in plasmonics. We applied the fifth order Savitzky–Golay filter with a nine-frame length and the Gaussian fitting process in MATLAB (R2016a, MathWorks) to reduce noise and determine more accurate peak positions (see Sections 6 and 7 of the Supporting Information and Figures S4 and S5).

**Fabrication of Implantable SERS Disks.** Silicon disks with a diameter of 1 mm and a thickness of  $300\ \mu\text{m}$  were patterned and etched from a Si wafer using the Bosch deep-reactive ion-etch process and attached onto a handling Si wafer using double-sided polyimide tape for further processing. 3D-stacked Au-NP clusters were fabricated on the disks using the same method described earlier. After processing, the SERS disks were detached from the Si-handling wafer and incubated in 1 mM MPBA solution for 5 hours. Then, we cast a C-shaped, 10 mm diameter PDMS platform in a plastic mold created using a 3D printer. Finally, the bottom of each SERS disk was attached onto a C-shaped PDMS platform, with the SERS active surface facing upward, using uncured PDMS, which was then cured at  $40^\circ\text{C}$  for 2 days. The arm width of the PDMS platform measured approximately 1 mm.

**Ex Vivo Measurements of Glucose Concentrations in Rabbit Eyes.** Six ex vivo eyes of New Zealand white rabbits

with diameters of approximately 2 cm were obtained from Sierra for Medical Science. A 2 mm corneal incision was made using Castroviejo scissors (Figure S7). A folded PDMS implant with a SERS disk was inserted into the anterior chamber and released, allowing it to unfold back to its original C shape. For reference measurement using a commercial electrochemical sensor (Accu-Chek Aviva Plus, Roche Diabetes Care Inc.), 5  $\mu$ L of aqueous humor was extracted from the anterior chamber of each ex vivo rabbit eye. The accuracy of the commercial sensor is  $\pm 15\%$  in 99% of the measurements for glucose concentrations above 4 mM.<sup>77</sup> The 2 mm corneal incision was sealed using medical-grade superglue. SERS signals were measured using the same Raman spectrometer under the same measurement conditions as the bench-top measurement. The measurements on the first two eyes were used for calibration.

## CONCLUSION

We have investigated Raman-mode constraining of MPBA resulting from glucose bonding; identified its underlying mechanism in simulation studies; and demonstrated quantitative, accurate glucose sensing in an on-chip microfluidic environment as well as in ex vivo rabbit eyes. Glucose–MPBA bonding modifies two of MPBA's Raman modes, resulting in a peak shift whose magnitude can be correlated to the ambient glucose concentration.

Our approach overcomes the naturally weak SERS signals of glucose, shows good resistance against enhancement variations that are inherent to SERS substrates, and could potentially allow monitoring of continuously changing glucose concentrations at levels observed in the aqueous humor and blood. Future studies will focus on developing implantable devices with improved Raman enhancement, signal-to-noise ratios, and concentration-readout speeds to pursue measurements in living animals and ultimately in humans. With further improvements, these results may open up a path for practical SERS-based in vivo glucose sensors.

## ASSOCIATED CONTENT

### Supporting Information

The Supporting Information is available free of charge on the ACS Publications website at DOI: 10.1021/acs.analchem.8b03420.

Experimental procedures, characteristics of the SERS substrate, enhancement-factor calculation, SERS spectra of MPBA and glucose-bonded MPBA, benchtop test of glucose concentration, signal processing for static Raman data, analytical glucose-sensing model, stability of the test over a 1 month period, ex vivo measurements of glucose in the anterior chambers of rabbit eyes, and glucose-sensing technologies (PDF)

Molecular vibration of the C–S-stretching-coupled C-ring-breathing mode of (OH<sup>−</sup>)-MPBA, C–S-stretching-coupled C-ring-bending mode of (OH<sup>−</sup>)-MPBA, and C–S-stretching-coupled C-ring-constrained-bending mode of (OH<sup>−</sup>)-MPBA bound with glucose (AVI)

## AUTHOR INFORMATION

### Corresponding Authors

\*E-mail: azayak@bgsu.edu (A.T.Z.).

\*E-mail: hchoo@caltech.edu (H. Choo).

## ORCID

Daejong Yang: 0000-0002-8774-5843

Shailabh Kumar: 0000-0001-5383-3282

Radwanul H. Siddique: 0000-0001-7494-5857

Alexey T. Zayak: 0000-0002-5741-3864

## Author Contributions

D.Y., J.O.L., and H. Choo conceived the study. D.Y. performed most of sample fabrication, experiments, and data processing under the supervision of H. Choo. S.A. conducted DFT simulations to identify the mode-shifting mechanism under the supervision of A.T.Z. J.O.L., H. Cho, and S.K. contributed at various stages during sample fabrication and measurements. R.H.S. contributed to the optical simulation and spectroscopy of the SERS substrates. S.K., V. N., and Y.-Z.Y. contributed to data-processing-algorithm development. D.Y. and H. Choo wrote the manuscript with S.A. and A.T.Z. and with a significant contribution from S.K. J.O.L., H. Cho., and Y.-Z.Y. also assisted with manuscript preparation. All authors discussed the results and commented on the manuscript.

## Notes

The authors declare no competing financial interest.

## ACKNOWLEDGMENTS

The authors thank Dr. Robert Grubbs (Department of Chemistry, California Institute of Technology) and Dr. Massimo Olivucci (Department of Chemistry, Bowling Green State University) for helpful discussions on boronic acid and computational modeling with solvents, respectively. The research was funded by a Samsung Grand Research Opportunity and the Heritage Medical Research Institute Inaugural Principle Investigator Program. Computational resources were provided by the Texas Advanced Computer Center (XSEDE Program) and the Ohio Supercomputer Center (OSC).

## REFERENCES

- (1) Narayan, K. M. V.; Gregg, E. W.; Engelgau, M. M.; Moore, B.; Thompson, T. J.; Williamson, D. F.; Vinicor, F. *Diabetes Care* **2000**, *23*, 1794–1798.
- (2) Kovatchev, B. P. *Nat. Rev. Endocrinol.* **2017**, *13*, 425–436.
- (3) Waldron-Lynch, F.; Herold, K. C. *Nat. Clin. Pract. Endocrinol. Metab.* **2009**, *5*, 82–83.
- (4) Lin, Y.; Lu, F.; Tu, Y.; Ren, Z. *Nano Lett.* **2004**, *4*, 191–195.
- (5) Besteman, K.; Lee, J.-O.; Wiertz, F. G. M.; Heering, H. A.; Dekker, C. *Nano Lett.* **2003**, *3*, 727–730.
- (6) Veisheh, O.; Tang, B. C.; Whitehead, K. A.; Anderson, D. G.; Langer, R. *Nat. Rev. Drug Discovery* **2015**, *14*, 45–57.
- (7) Yu, H. Y.; Xu, M. Q.; Yu, S. H.; Zhao, G. C. *Int. J. Electrochem. Sci.* **2013**, *8*, 8050–8057.
- (8) Reitz, E.; Jia, W. Z.; Gentile, M.; Wang, Y.; Lei, Y. *Electroanalysis* **2008**, *20*, 2482–2486.
- (9) Heinemann, L. J. *Diabetes Sci. Technol.* **2008**, *2*, 919–921.
- (10) Emaminejad, S.; Gao, W.; Wu, E.; Davies, Z. A.; Nyein, H. Y.; Challa, S.; Ryan, S. P.; Fahad, H. M.; Chen, K.; Shahpar, Z.; Talebi, S.; Milla, C.; Javey, A.; Davis, R. W. *Proc. Natl. Acad. Sci. U. S. A.* **2017**, *114*, 4625–4630.
- (11) Gao, W.; Emaminejad, S.; Nyein, H. Y.; Challa, S.; Chen, K. V.; Peck, A.; Fahad, H. M.; Ota, H.; Shiraki, H.; Kiriya, D.; Lien, D. H.; Brooks, G. A.; Davis, R. W.; Javey, A. *Nature* **2016**, *529*, 509–514.
- (12) Lee, H.; Choi, T. K.; Lee, Y. B.; Cho, H. R.; Ghaffari, R.; Wang, L.; Choi, H. J.; Chung, T. D.; Lu, N. S.; Hyeon, T.; Choi, S. H.; Kim, D. H. *Nat. Nanotechnol.* **2016**, *11*, 566–572.



- (13) Lee, H.; Song, C.; Hong, Y. S.; Kim, M. S.; Cho, H. R.; Kang, T.; Shin, K.; Choi, S. H.; Hyeon, T.; Kim, D. H. *Sci. Adv.* **2017**, *3*, No. e1601314.
- (14) Tierney, M. J.; Kim, H. L.; Burns, M. D.; Tamada, J. A.; Potts, R. O. *Electroanalysis* **2000**, *12*, 666–671.
- (15) Sakaguchi, K.; Hirota, Y.; Hashimoto, N.; Ogawa, W.; Hamaguchi, T.; Matsuo, T.; Miyagawa, J.-I.; Namba, M.; Sato, T.; Okada, S.; Tomita, K.; Matsuhisa, M.; Kaneto, H.; Kosugi, K.; Maegawa, H.; Nakajima, H.; Kashiwagi, A. *J. Diabetes Sci. Technol.* **2013**, *7*, 678–688.
- (16) Toghiani, K. E.; Compton, R. G. *Int. J. Electrochem. Sci.* **2010**, *5*, 1246–1301.
- (17) Beers, M. H.; Fletcher, A. J. *The Merck Manual of Medical Information*, 2nd ed.; Merck Research Laboratories: Whitehouse Station, NJ, 2003.
- (18) Vaddiraju, S.; Burgess, D. J.; Tomazos, I.; Jain, F. C.; Papadimitrakopoulos, F. J. *J. Diabetes Sci. Technol.* **2010**, *4*, 1540–1562.
- (19) Weiss, R.; Yegorchikov, Y.; Shusterman, A.; Raz, I. *Diabetes Technol. Ther.* **2007**, *9*, 68–74.
- (20) Sapozhnikova, V. V.; Kuranov, R. V.; Cicenaitis, I.; Esenaliev, R. O.; Prough, D. S. *J. Biomed. Opt.* **2008**, *13*, 021112.
- (21) Cameron, B. D.; Anumula, H. *Diabetes Technol. Ther.* **2006**, *8*, 156–164.
- (22) Rounds, R. M.; Ibey, B. L.; Beier, H. T.; Pishko, M. V.; Cote, G. L. *J. Fluoresc.* **2007**, *17*, 57–63.
- (23) Oliver, N. S.; Toumazou, C.; Cass, A. E. G.; Johnston, D. G. *Diabetic Med.* **2009**, *26*, 197–210.
- (24) Liu, N.; Mesch, M.; Weiss, T.; Hentschel, M.; Giessen, H. *Nano Lett.* **2010**, *10*, 2342–2348.
- (25) Amerov, A. K.; Chen, J.; Small, G. W.; Arnold, M. A. *Anal. Chem.* **2005**, *77*, 4587–4594.
- (26) Feng, J.; Siu, V. S.; Roelke, A.; Mehta, V.; Rhieu, S. Y.; Palmore, G. T. R.; Pacifici, D. *Nano Lett.* **2012**, *12*, 602–609.
- (27) McCreery, R. L. *Raman Spectroscopy for Chemical Analysis*; John Wiley & Sons: New York, 2000.
- (28) Campion, A.; Kambhampati, P. *Chem. Soc. Rev.* **1998**, *27*, 241–250.
- (29) Willets, K. A.; Van Duyne, R. P. *Annu. Rev. Phys. Chem.* **2007**, *58*, 267–297.
- (30) Wang, D.; Zhu, W.; Best, M. D.; Camden, J. P.; Crozier, K. B. *Nano Lett.* **2013**, *13*, 2194–2198.
- (31) Li, Z.-Y.; Xia, Y. *Nano Lett.* **2010**, *10*, 243–249.
- (32) Ahmed, A.; Gordon, R. *Nano Lett.* **2012**, *12*, 2625–2630.
- (33) Cho, H.; Baker, B. R.; Wachsmann-Hogiu, S.; Pagba, C. B.; Laurence, T. A.; Lane, S. M.; Lee, L. P.; Tok, J. B.-H. *Nano Lett.* **2008**, *8*, 4386–4390.
- (34) Kang, T.; Yoo, S. M.; Yoon, I.; Lee, S. Y.; Kim, B. *Nano Lett.* **2010**, *10*, 1189–1193.
- (35) Lyandres, O.; Shah, N. C.; Yonzon, C. R.; Walsh, J. T.; Glucksberg, M. R.; Van Duyne, R. P. *Anal. Chem.* **2005**, *77*, 6134–6139.
- (36) Ma, K.; Yuen, J. M.; Shah, N. C.; Walsh, J. T.; Glucksberg, M. R.; Van Duyne, R. P. *Anal. Chem.* **2011**, *83*, 9146–9152.
- (37) Sharma, B.; Bugga, P.; Madison, L. R.; Henry, A. I.; Blaber, M. G.; Greeneltch, N. G.; Chiang, N. H.; Mrksich, M.; Schatz, G. C.; Van Duyne, R. P. *J. Am. Chem. Soc.* **2016**, *138*, 13952–13959.
- (38) Tong, L. M.; Xu, H. X.; Kall, M. *MRS Bull.* **2014**, *39*, 163–168.
- (39) Marotta, N. E.; Beavers, K. R.; Bottomley, L. A. *Anal. Chem.* **2013**, *85*, 1440–1446.
- (40) Sun, X. C.; Stagon, S.; Huang, H. C.; Chen, J.; Lei, Y. *RSC Adv.* **2014**, *4*, 23382–23388.
- (41) Li, S. S.; Zhou, Q.; Chu, W. Y.; Zhao, W.; Zheng, J. W. *Phys. Chem. Chem. Phys.* **2015**, *17*, 17638–17645.
- (42) Kitagawa, T.; Tashiro, K.; Yabuki, K. *J. Polym. Sci., Part B: Polym. Phys.* **2002**, *40*, 1269–1280.
- (43) Roelli, P.; Galland, C.; Piro, N.; Kippenberg, T. *Nat. Nanotechnol.* **2016**, *11*, 164–169.
- (44) Guerrini, L.; Pazos, E.; Penas, C.; Vazquez, M. E.; Mascarenas, J. L.; Alvarez-Puebla, R. A. *J. Am. Chem. Soc.* **2013**, *135*, 10314–10317.
- (45) Zhuang, H. J.; Zhu, W. F.; Yao, Z. Y.; Li, M.; Zhao, Y. L. *Talanta* **2016**, *153*, 186–190.
- (46) Chen, L.; Zhao, Y.; Wang, Y. X.; Zhang, Y. J.; Liu, Y.; Han, X. X.; Zhao, B.; Yang, J. H. *Analyst* **2016**, *141*, 4782–4788.
- (47) Dong, J.; Liu, T.; Meng, X. M.; Zhu, J. Y.; Shang, K.; Ai, S. Y.; Cui, S. L. *J. Solid State Electrochem.* **2012**, *16*, 3783–3790.
- (48) Sakalak, H.; Ulasan, M.; Yavuz, E.; Camli, S. T.; Yavuz, M. S. *J. Nanopart. Res.* **2014**, *16*, 2767.
- (49) James, T. D.; Phillips, M. D.; Shinkai, S. *Boronic Acids in Saccharide Recognition*, 1st ed.; Royal Society of Chemistry: Cambridge, U.K., 2006.
- (50) Lorand, J. P.; Edwards, J. O. *J. Org. Chem.* **1959**, *24*, 769–774.
- (51) Springsteen, G.; Wang, B. H. *Chem. Commun.* **2001**, *0*, 1608–1609.
- (52) Yang, D.; Cho, H.; Koo, S.; Vaidyanathan, S. R.; Woo, K.; Yoon, Y.; Choo, H. *ACS Appl. Mater. Interfaces* **2017**, *9*, 19092–19101.
- (53) Cho, H.; Kumar, S.; Yang, D.; Vaidyanathan, S.; Woo, K.; Garcia, I.; Shue, H. J.; Yoon, Y.; Ferreri, K.; Choo, H. *ACS Sens* **2018**, *3*, 65–71.
- (54) Orendorff, C. J.; Gole, A.; Sau, T. K.; Murphy, C. *Anal. Chem.* **2005**, *77*, 3261–3266.
- (55) Sun, D.; Qi, G. H.; Xu, S. P.; Xu, W. Q. *RSC Adv.* **2016**, *6*, 53800–53803.
- (56) Sen, D. K.; Sarin, G. S. *Br. J. Ophthalmol.* **1980**, *64*, 693–695.
- (57) Davies, P. D.; Duncan, G.; Pynsent, P. B.; Arber, D. L.; Lucas, V. A. *Exp. Eye Res.* **1984**, *39*, 605–609.
- (58) Schrader, W. F.; Stehberger, B.; Meuer, P. *Invest. Ophthalmol. Vis. Sci.* **2002**, *43*, 3263.
- (59) Springsteen, G.; Wang, B. H. *Tetrahedron* **2002**, *58*, 5291–5300.
- (60) Kong, K. V.; Ho, C. J. H.; Gong, T. X.; Lau, W. K. O.; Olivo, M. *Biosens. Bioelectron.* **2014**, *56*, 186–191.
- (61) Sun, F.; Bai, T.; Zhang, L.; Ella-Menye, J.-R.; Liu, S.; Nowinski, A. K.; Jiang, S.; Yu, Q. *Anal. Chem.* **2014**, *86*, 2387–2394.
- (62) Kawasaki, T.; Akanuma, H.; Yamanouchi, T. Y. *Diabetes Care* **2002**, *25*, 353–357.
- (63) Harding, J. J.; Hassett, P.; Rixon, K. C.; Bron, A. J.; Harvey, D. J. *Curr. Eye Res.* **1999**, *19*, 131–136.
- (64) Bélanger, M. C.; Marois, Y. J. *J. Biomed. Mater. Res.* **2001**, *58*, 467–477.
- (65) Peterson, S. L.; McDonald, A.; Gourley, P. L.; Sasaki, D. Y. *J. Biomed. Mater. Res.* **2005**, *72A*, 10–18.
- (66) Kim, S. H.; Moon, J. H.; Kim, J. H.; Jeong, S. M.; Lee, S. H. *Biomed. Eng. Lett.* **2011**, *1*, 199–203.
- (67) Lo, R.; Li, P. Y.; Saati, S.; Agrawal, R.; Humayun, M. S.; Meng, E. *Lab Chip* **2008**, *8*, 1027–1030.
- (68) Humayun, M.; Santos, A.; Altamirano, J. C.; Ribeiro, R.; Gonzalez, R.; de la Rosa, A.; Shih, J.; Pang, C.; Jiang, F.; Calvillo, P.; Huculak, J.; Zimmerman, J.; Caffey, S. *Transl. Vis. Sci. Technol.* **2014**, *3*, 5.
- (69) Goel, M.; Picciani, R. G.; Lee, R. K.; Bhattacharya, S. K. *Open Ophthalmol. J.* **2010**, *4*, 52–59.
- (70) Baca, J. T.; Finegold, D. N.; Asher, S. A. *Ocul. Surf.* **2007**, *5*, 280–293.
- (71) Lee, J. O.; Narasimhan, V.; Du, J.; Ndjamen, B.; Sretavan, D.; Choo, H. *Adv. Healthcare Mater.* **2017**, *6*, 1601356.
- (72) Algreve, P. V.; Torstensson, P. A. L.; Tengroth, B. M. *Invest. Ophthalmol. Vis. Sci.* **1993**, *34*, 349–354.
- (73) World Health Organization. *Definition and Diagnosis of Diabetes Mellitus and Intermediate Hyperglycaemia*; WHO Document Production Services: Geneva, Switzerland, 2006. [http://www.who.int/diabetes/publications/diagnosis\\_diabetes2006/en/](http://www.who.int/diabetes/publications/diagnosis_diabetes2006/en/) (accessed Sept 9, 2018).
- (74) Frisch, M. J.; Trucks, G. W.; Schlegel, H. B.; Scuseria, G. E.; Robb, M. A.; Cheeseman, J. R.; Scalmani, G.; Barone, V.; Mennucci,

B.; Petersson, G. A.; Nakatsuji, H.; Caricato, M.; Li, X.; Hratchian, H. P.; Izmaylov, A. F.; Bloino, J.; Zheng, G.; Sonnenberg, J. L.; Hada, M.; Ehara, M.; Toyota, K.; Fukuda, R.; Hasegawa, J.; Ishida, M.; Nakajima, T.; Honda, Y.; Kitao, O.; Nakai, H.; Vreven, T.; Montgomery, J. A., Jr.; Peralta, J. E.; Ogliaro, F.; Bearpark, M.; Heyd, J. J.; Brothers, E.; Kudin, K. N.; Staroverov, V. N.; Kobayashi, R.; Normand, J.; Raghavachari, K.; Rendell, A.; Burant, J. C.; Iyengar, S. S.; Tomasi, J.; Cossi, M.; Rega, N.; Millam, J. M.; Klene, M.; Knox, J. E.; Cross, J. B.; Bakken, V.; Adamo, C.; Jaramillo, J.; Gomperts, R.; Stratmann, R. E.; Yazyev, O.; Austin, A. J.; Cammi, R.; Pomelli, C.; Ochterski, J. W.; Martin, R. L.; Morokuma, K.; Zakrzewski, V. G.; Voth, G. A.; Salvador, P.; Dannenberg, J. J.; Dapprich, S.; Daniels, A. D.; Farkas, O.; Foresman, J. B.; Ortiz, J. V.; Cioslowski, J.; Fox, D. J. *Gaussian 09*; Gaussian, Inc.: Wallingford, CT, 2009.

(75) Becke, A. D. *J. Chem. Phys.* **1993**, *98*, 5648–5652.

(76) Alkauskas, A.; Baratoff, A.; Bruder, C. *J. Phys. Chem. A* **2004**, *108*, 6863–6868.

(77) Freckmann, G.; Schmid, C.; Baumstark, A.; Pleus, S.; Link, M.; Haug, C. *J. Diabetes Sci. Technol.* **2012**, *6*, 1060–1075.